

Vacancy-Ordered Double Perovskite Cs_2TeI_6 Thin Films for Optoelectronics

Isabel Vázquez-Fernández,* Silvia Mariotti, Oliver S. Hutter, Max Birkett, Tim D. Veal, Theodore D. C. Hobson, Laurie J. Phillips, Lefteris Danos, Pabitra K. Nayak, Henry J. Snaith, Wei Xie, Matthew P. Sherburne, Mark Asta, and Ken Durose



Cite This: *Chem. Mater.* 2020, 32, 6676–6684



Read Online

ACCESS |



Metrics & More

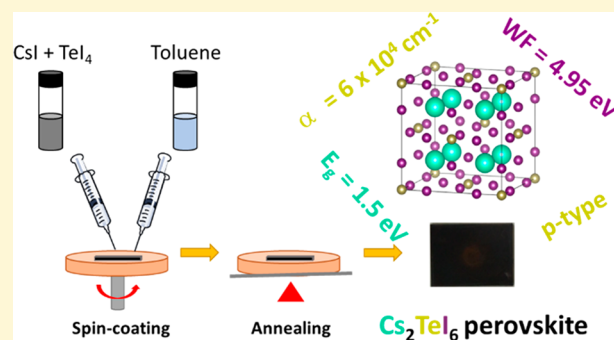


Article Recommendations



Supporting Information

ABSTRACT: Alternatives to lead- and tin-based perovskites for photovoltaics and optoelectronics are sought that do not suffer from the disadvantages of toxicity and low device efficiency of present-day materials. Here we report a study of the double perovskite Cs_2TeI_6 , which we have synthesized in the thin film form for the first time. Exhaustive trials concluded that spin coating CsI and TeI_4 using an antisolvent method produced uniform films, confirmed as Cs_2TeI_6 by XRD with Rietveld analysis. They were stable up to 250 °C and had an optical band gap of ~ 1.5 eV, absorption coefficients of $\sim 6 \times 10^4$ cm^{-1} , carrier lifetimes of ~ 2.6 ns (unpassivated 200 nm film), a work function of 4.95 eV, and a p-type surface conductivity. Vibrational modes probed by Raman and FTIR spectroscopy showed resonances qualitatively consistent with DFT *Phonopy*-calculated spectra, offering another route for phase confirmation. It was concluded that the material is a candidate for further study as a potential optoelectronic or photovoltaic material.



INTRODUCTION

Following the first publication reporting a hybrid organic–inorganic perovskite solar cell in 2009, when a $\text{CH}_3\text{NH}_3\text{PbI}_3$ absorber layer resulted in a 3.5% efficiency,¹ and breakthroughs delivering >10% efficient cells in 2012,^{2,3} the field has accelerated rapidly. In the past few years the efficiency has been increased to over 25.2%,⁴ which is comparable to silicon photovoltaics. Unfortunately, these outstanding efficiencies can only be achieved with the use of lead which has known toxicity issues, and the devices demonstrate relatively poor stability in contact with moisture, UV light, and elevated temperatures.^{5–7} Niu et al.⁸ summarized the principal stability issues for lead-based perovskites arising in device structures, during solution processing and fundamentally in terms of the thermal stability of the crystal structure and the selection of their chemical components. Although significant improvements have been made moving away from the archetypical methylammonium cation, to formamidinium,^{9,10} the move to a completely inorganic compound could enable a further transformational improvement in thermal stability. Overall, current challenges for the field lie in the improvement of the stability of organic–inorganic lead halide perovskites, and debate remains concerning the environmental impact of the lead content.

Perovskites have the formula ABX_3 , where A is an organic or inorganic ion, B is a metal, and X is a halide ion. Many studies have explored substitutions on the A-site to form a more stable phase, but these changes seem to be less influential on the

optoelectronic properties than substituting the halide. For example, Noh et al.¹¹ have found that using smaller halide ions, e.g., bromide rather than iodide, increases the stability for electrostatic reasons. However, fewer studies have investigated substituting the B-site metal ion alone to replace the lead.

Among the lead-free perovskites, the most promising up to now are the tin-based iodide materials. The first study with tin, to form a methylammonium tin iodide absorber ($\text{CH}_3\text{NH}_3\text{SnI}_3$), was published by Noel et al.¹² and reported efficiencies over 6%. However, stability issues under ambient conditions, much more extreme than those for lead-iodide perovskites, exist. Specifically, the reduced stability of the Sn^{2+} oxidation state relative to Pb^{2+} has the capacity to introduce harmful deep levels into tin based perovskites, and their efficiencies have lagged significantly behind those of lead-based devices, which are known to be defect tolerant. In contrast to $\text{CH}_3\text{NH}_3\text{SnI}_3$ and CsSnI_3 , the double perovskite Cs_2SnI_6 with tin in a 4+ oxidation state exhibits enhanced stability to air and moisture.¹³ Cs_2SnI_6 has been shown to be a functional hole conductor, when employed in dye-sensitized solar cells.¹⁴ In

Received: May 22, 2020

Revised: July 9, 2020

Published: July 9, 2020



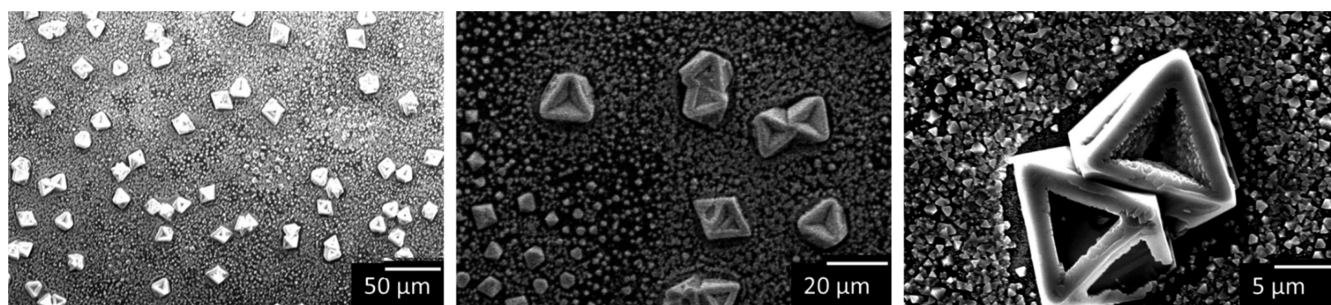


Figure 1. SEM images of Cs_2TeI_6 crystals on films formed by one-step spin coating using DMSO.

addition, Cs_2SnI_6 has been reported with band gaps in the range 1.3–1.6 eV making it potentially suitable for use as an absorber layer in photovoltaics.^{13–15} The power conversion efficiency (PCE) of Cs_2SnI_6 solar cells in a device with nanostructured ZnO has been reported to be about 1% to date.¹⁶ Its crystal structure is related to the common ABX_3 perovskite structure by removing half of the B ions (Sn^{4+}) resulting in a vacancy-ordered double perovskite. The A_2BX_6 structure has been doped by impurity ions to tune the electronic and optical properties,¹⁷ although no high-performance devices have yet been reported.

While Tin is of itself less toxic than lead, a full life cycle analysis indicates that other issues could arise from the substitution of lead with tin. From an evaluation of the active and partner layers and including mineral extraction, manufacture, service, materials costs, and end of life issues, it was concluded that tin-based devices could, overall, contribute greater human and freshwater ecotoxicity than lead ones.¹⁸ While that study was based on earlier device designs and performance values, it nevertheless highlights the need for alternative to lead and tin.¹⁹

Here, we report tellurium as a potential replacement element for lead and tin on the B-site in perovskites for optoelectronic applications. Studies of tellurium are mainly focused on tellurite (TeO_3^{2-}), tellurate (TeO_4^{2-}), organic tellurides (Te^{2-}),²⁰ and the semiconducting material, CdTe.²¹ The tetravalent Te^{4+} cation has the same number of electrons as Sn^{2+} and the same valence electronic configuration as Pb^{2+} . Also, Te^{4+} , Sn^{2+} , and Pb^{2+} have similar electronegativities although the ionic radius of Te^{4+} is slightly smaller (97 pm) compared to Sn^{2+} (110 pm) and Pb^{2+} (119 pm).²² The magnitude of the ionic radius is an important factor that determines the tolerance factor²³ and, hence, the formation of a stable perovskite structure. Since the ionic radii are broadly comparable, it may be expected that tellurium can substitute tin or lead in perovskites structures.

In stark contrast to the known high toxicity of lead, tellurium is only mildly toxic, and it is not reported to be carcinogenic.²⁴ All of these features make tellurium a perfect candidate for replacing lead. Nonetheless, one must emphasize that the toxic effect of this element must be related to the chemical composition of the specific compound. Hence although the available information is encouraging, tellurium toxicity and its potential harmful effects do need further investigation. Several theoretical papers have predicted that Cs_2TeI_6 is expected to have useful properties for PV devices,^{17,25} but there are no reports of experimental results on thin films, which is the subject of the present paper.

Cs_2TeI_6 has been synthesized previously by modification of the solution method proposed by Lee et al.¹³ for Cs_2SnI_6 and

using a mixed solution of the two precursors. A second solution of heated TeI_4 in ethanol and HI was added to the first solution giving rise to a black precipitate that was finally purified yielding Cs_2TeI_6 . It was also synthesized by Peresh et al.²⁶ to study stability regions at different molar ratios using thermal analysis. The melting temperature coincided with the stoichiometric compositions of the precursors.

Here, we propose a different synthetic procedure using stoichiometric amounts of CsI and TeI_4 . When combined with an antisolvent treatment, this creates extremely homogeneous, dense, and pinhole-free perovskite Cs_2TeI_6 thin films by increasing the nucleation density during spin coating. We report extensive characterization of the film structure, morphology, stability, work function, fluorescence lifetime, and simulated and experimental IR and Raman spectra. To the best of our knowledge, this is the first publication reporting a Cs_2TeI_6 thin film and its optoelectronic properties.

RESULTS AND DISCUSSION

One- and Two-Step Spin Coating Cs_2TeI_6 Synthesis and Film Formation. We made an exhaustive survey of the parameters using a combined solution synthesis and spin coating of Cs_2TeI_4 films directly from CsI and TeI_4 in a single step, i.e., with both precursors being present in the solution simultaneously. The variables investigated were the type of solvent (DMSO, DMF, and DMSO/DMF mixture), number of layers (1–4), precursor weight fraction (14, 26, 30, 35, 47, and 53 wt %), precursor molar ratio CsI: TeI_4 (2:1, 1:1, and 1:1.5), solution temperature (RT and 50 °C), spin coating conditions (static/dynamic, rpm, and time), annealing temperatures (50–300 °C), and annealing time (1 min–10 min).

A total of over 50 experimental conditions were tested and over 500 films were made. Figure S1 illustrates the experimental procedure for Cs_2TeI_6 film fabrication and the quality of the films using different solvents. The scanning electron microscope (SEM) images of the Cs_2TeI_6 films shown in Figure 1 reveal that the films comprise large crystals ($\sim 5 \mu\text{m}$) surrounded by smaller crystals ($\sim 1.4 \mu\text{m}$), both having the same triangular bipyramidal shape. The thickness of the films was examined by atomic force microscopy (AFM) and found to be $\sim 235 \text{ nm}$, although these one-step films were discontinuous.

The main findings from the survey of one-step synthesis and spin coating conditions were as follows:

- DMSO gave the most uniform films.
- The optimum number of spin cycles was two, as this yielded $\sim 500 \text{ nm}$ crystalline films displaying clear optical bandgaps, making them suitable for PV devices.

- iii. The highest concentration in the solution of the precursors trialed (53 wt %) yielded the highest quality films, showing strong optical absorption compared to lower concentrations.
- iv. The 2:1 molar ratio between CsI and TeI₄ was required to form Cs₂TeI₆.
- v. Dynamic spin coating deposition was necessary for perovskite film formation, as revealed by X-ray diffraction (XRD) and SEM. Drop casting did not lead to perovskite. No warming of the solution was necessary.
- vi. Annealing temperatures above 250 °C led to the decomposition of the Cs₂TeI₆, causing the films to change from black to white, possibly due to the loss of TeI₄ which is more volatile than CsI. At $T > 150$ °C, the films started to look patchy, so annealing was carried out at 100 °C.
- vii. The annealing time does not play an important role in the Cs₂TeI₆ perovskite crystallization process, as only small differences were found by changing this variable.

From the above survey, the optimum conditions for deposition of thin film Cs₂TeI₆ (by spin coating from DMSO) were identified and are described in the [Experimental and Computational Details](#). The phase purity was verified by XRD, as explained below.

In addition to the one-step deposition process, two-step formation of Cs₂TeI₆ films was also attempted in which TeI₄ and CsI were individually spin coated from solution and annealed to form films. (This mirrors the two-step process used to form the organic–inorganic hybrid perovskite CH₃NH₃PbI₃ which is capable of yielding devices with a PCE of 15%).²⁷ Here the solvent was DMSO, and the TeI₄ preceded the CsI deposition. However, the resulting deposits were extremely inhomogeneous, and this method was discontinued.

Formation of Cs₂TeI₆ Films by Spin Coating with an Antisolvent. Since the films prepared above using the one-step spin coating process were inhomogeneous at the microscopic level and contained grains having disparate sizes, an alternative “antisolvent” spin coating method was investigated. Addition of an antisolvent during spinning reduces the solubility of the solute, forcing supersaturation and increasing the density of the nucleation sites.^{28,29}

Here we investigated the action of dichloromethane, diethyl ether, chlorobenzene, and toluene as antisolvents. The procedure was to spin coat using a solution of TeI₄ and CsI in DMSO as before but to drip the antisolvent (200 μL) into the center of the substrate at the same time, followed by annealing at 110 °C for 10 min. Of the antisolvents tested, the best films were obtained using toluene. Comparisons of the films prepared with and without the antisolvent are shown in [Figure 2a–d](#). Its use yields visibly more homogeneous films without pinholes, and the SEM micrographs show that the films are smoother and do not contain the 5 μm protruding grains generated by the one-step process as shown in [Figure 1](#).

The overall outcome of the film preparation study in this work is that the most homogeneous films of Cs₂TeI₆ were prepared by spin coating of TeI₄ and CsI from DMSO with the addition of toluene as an antisolvent. Photographs of the Cs₂TeI₆ thin films prepared without antisolvent and using a toluene antisolvent are shown in [Figure S1](#).

XRD, FTIR, and Raman Spectroscopy. XRD (θ – 2θ) was used to confirm the formation of Cs₂TeI₆ and to explore the

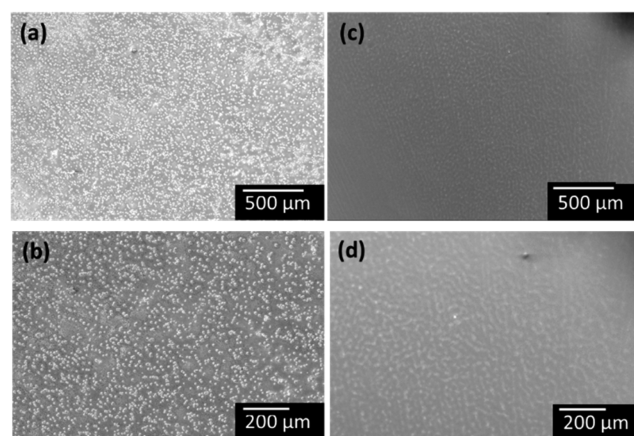


Figure 2. (a, b) SEM images of Cs₂TeI₆ crystals formed without antisolvent and (c, d) using toluene as an antisolvent.

preferred orientation and grain size effects in the films. [Figure 3a](#) shows a normalized comparison of the spectrum for a film of Cs₂TeI₆ compared to those for spin coated films of the CsI and TeI₄ precursors alone. The Cs₂TeI₆ film is clearly distinct from those for the precursors indicating formation of a new compound. Moreover, it contains only peaks present in the reference spectrum for bulk powder.

The data are consistent with those for Cs₂TeI₆ as listed in the International Crystal Structure Database (ICSD) record 38105, confirming the film to have the intended composition. This was further confirmed by Rietveld refinements³⁰ ([Figure S2](#)) of patterns for Cs₂TeI₆ films both with and without the antisolvent treatment.

This showed a single crystalline cubic phase for each (space group $Fm\bar{3}m$) having a lattice parameter of 11.6775 Å for films with antisolvent and 11.6754 Å without antisolvent. The ICSD reference pattern is shown in [Figure 3b](#) alongside patterns for films formed both using DMSO alone and with the addition of toluene as an antisolvent. Differences in the intensities of these two compared to those in the random powder ICSD spectrum (including absences) are due to preferred orientations (texture) in the films. While the straightforward one-step film formed with DMSO had one major peak (222), i.e., a strong preferred orientation, use of the toluene antisolvent encouraged a higher number of peaks indicating more randomized crystal texture. This was confirmed quantitatively with Harris texture coefficient analysis³¹ as shown in [Table 1](#). The coefficients for films prepared without antisolvent show enhanced values for the close packed planes (111) and (222) and a relatively high standard deviation, while those for the antisolvent prepared films show high values for a greater number of peaks and a correspondingly low standard deviation. It was also seen that the simple one-step DMSO process gave sharp diffraction peaks which are broadened by inclusion of the antisolvent, as shown in [Figure 3b](#) for toluene and [Figure 3c](#) for the other antisolvents. While this is most likely to be due to a reduction in particle size, it was not confirmed quantitatively from the XRD FWHMs since there were too few peaks to make a full Williamson–Hall plot that would distinguish particle size from strain.

By carrying out FTIR on the films in the range 1500–4000 cm⁻¹ we were able to determine that the Cs₂TeI₆ films did not contain any of the absorption features expected for either the solvent (DMSO) or, when used, the antisolvent (toluene).

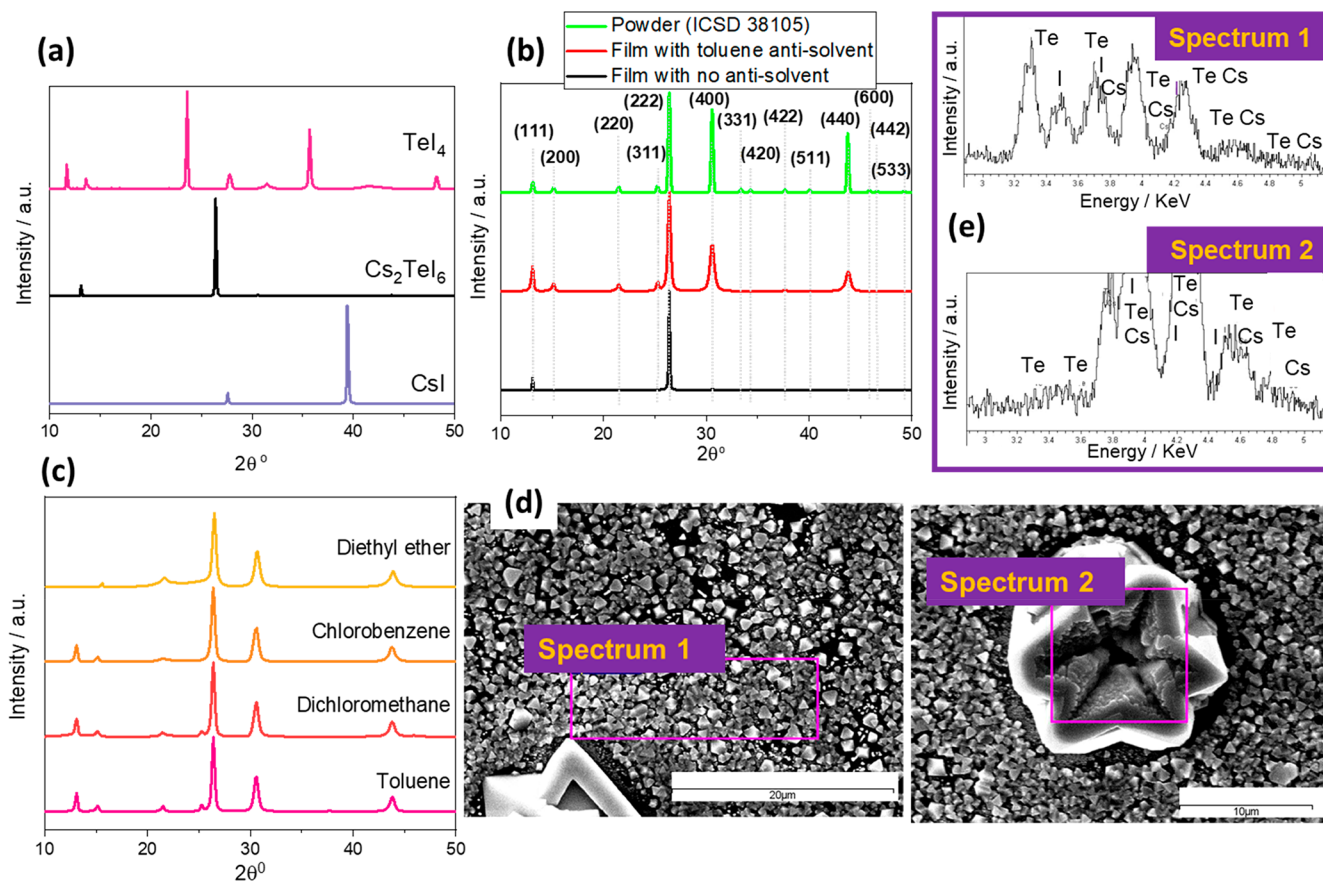


Figure 3. (a) XRD patterns of CsI, TeI_4 , and Cs_2TeI_6 thin films. (b) XRD spectra of Cs_2TeI_6 powder tabulated in the International Crystal Structure Database (ICSD) 38105 (top), Cs_2TeI_6 thin film prepared without (middle) and including (bottom) toluene antisolvent treatment. (c) XRD Cs_2TeI_6 thin film treated with different antisolvents. (d) SEM images of different parts of the Cs_2TeI_6 thin film. (e) EDX results from the areas in (d).

Table 1. Texture Coefficients, C_{hkl} , and their Standard Deviations (σ) for Typical Films of Cs_2TeI_6 Formed with and without Antisolvent

	C_{111}	C_{200}	C_{220}	C_{311}	C_{222}	C_{400}	C_{331}	C_{420}	C_{422}	C_{511}	C_{440}	C_{600}	C_{442}	C_{533}	σ
no antisolvent	5.43	0.42	0.34	0.41	4.04	0.08	0.36	0.38	0.25	1.25	0.03	0.23	0.39	0.41	1.73
antisolvent	3.48	2.01	2.01	1.88	1.3	0.67	0.11	0.12	0.67	0.08	0.4	0.07	0.12	1.07	1.03

Hence, we were able to determine that the films contained no residual solvent that could affect their microstructure. Overall though it may be speculated that the effect of the antisolvent is to increase the nucleation density in the film. This would reasonably be expected to randomize the crystal texture and to reduce the particle size.

It would also act to eliminate the formation of the large crystallites in one-step grown films of the type shown in Figure 1. Finally, we present SEM images of the film and one of the large crystallites (Figure 3d) and EDX spectra from both (Figure 3e). Composition data extracted from the EDX spectra are shown in Table 2 and confirm that the approximate proportions of Cs, Te, and I expected for Cs_2TeI_6 were present, further confirming formation of the compound.

FTIR and Raman spectroscopies were used here as alternative techniques to monitor the perovskites and confirm their symmetries. In some cases the perovskite structure is distorted, and the symmetry is lowered from cubic to tetragonal or monoclinic.³² The phonon dispersion relation calculated with DFT using the finite displacement method for Cs_2TeI_6 in the $Fm\bar{3}m$ space group is given in Figure S3. It

Table 2. Results of EDX Analysis for Cs_2TeI_6 Films Prepared by Spin Coating from DMSO and Shown in Figure 3

	atomic ratio			
	Cs	Te	I	
ideal	2	1	6	
EDX	spectrum 1	1.8	1.4	5.8
	spectrum 2	2.0	1.1	5.9

matches those in the Materials Project³³ and Togo's phonon calculation³⁴ well.

Factor group analysis (first order atomic displacement vectors respecting space group $Fm\bar{3}m$) predicts 24 zone-center optical phonon modes with the following symmetries:

$$\Gamma = A_{1g} + E_g + T_{1g} + 2T_{2g} + 3T_{1u} + T_{2u}$$

Modes with T_{1g} and T_{2u} symmetries are silent (not seen in either Raman or IR spectra), while selection rules arising from the Cs_2TeI_6 crystal inversion center create mutually exclusive

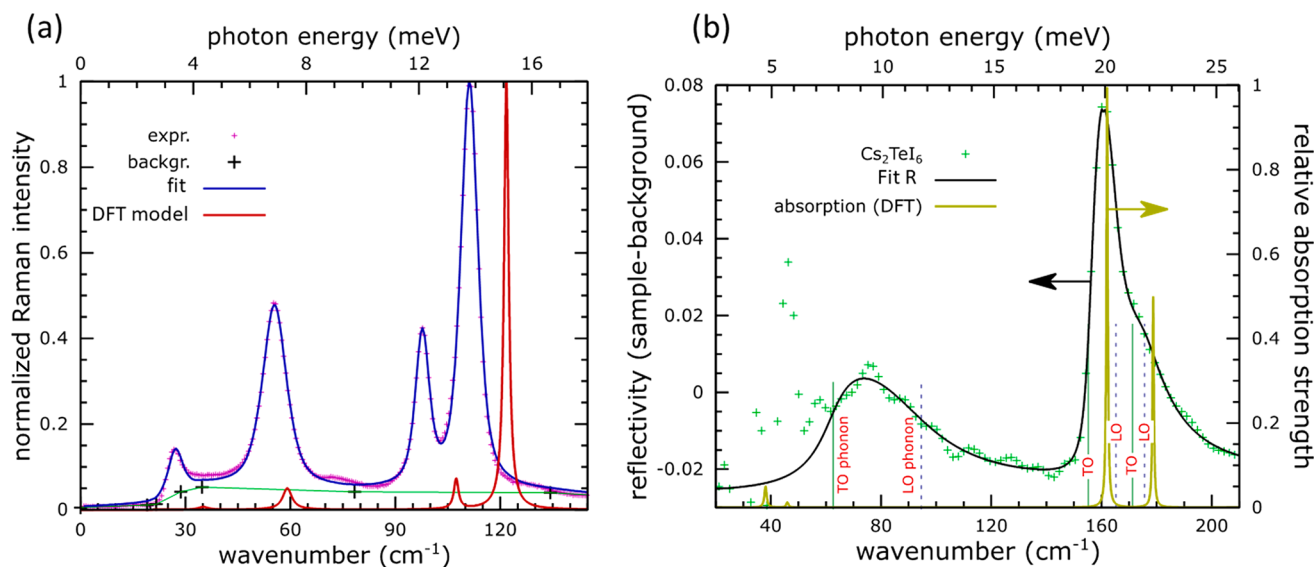


Figure 4. (a) Raman spectrum of the Cs_2TeI_6 film using antisolvent. Experimental data were fitted with a Gaussian–Lorentzian line shape model. The DFT-simulated Raman spectrum shown alongside was broadened using simulated phonon line widths at 300 K between 20 and 150 cm^{-1} . (b) Experimental, fitted, and DFT-simulated FTIR of a Cs_2TeI_6 film. The experimental spectrum (300 K) is fitted to a reflectivity model that builds the dielectric function from three harmonic oscillators fitted to the baseline-subtracted experimental data. The DFT-calculated IR-active phonon lines are shown and are from optical absorption calculations.

Raman and IR modes: Raman-active modes are IR-forbidden and vice versa. Therefore,

$$\Gamma_{\text{opt}}(k=0) = A_{1g}(\text{R}) + E_g(\text{R}) + 2T_{2g}(\text{R}) + 3T_{1u}(\text{IR})$$

Visualization of the phonon eigenvectors indicates that the three IR active vibration modes, all T_{1u} in order of increasing frequency, correspond to vibrations of octahedra $[\text{TeI}_6]^{2-}$ against Cs^+ cations,³⁵ I–Te–I bending, and Te–I stretching, respectively. The four Raman vibrations include symmetric A_{1g} and asymmetric E_g stretching (ν) of Te–I, an asymmetric T_{2g} bending (δ) of I–Te–I, and a T_{2g} stretching (ν^{\perp}) of the Cs atoms.³⁵ Figure 4a shows the Raman spectra for Cs_2TeI_6 including the experimental data and the fit to it and also a DFT-simulated spectrum, revealing four bands below 150 cm^{-1} .

A good fit was achieved after background subtraction (via levels unconfused with bands) using a common Gaussian–Lorentzian line shape with identical component line widths and magnitudes, giving strong modes at 111.212 (13) cm^{-1} , 97.73 (3) cm^{-1} , and 55.46 (4) cm^{-1} and a weak mode at 27.10 (12) cm^{-1} . The DFT *Phonopy* calculated Raman spectrum shows the four Raman active peaks indicated by group theory, with line positions and relative intensities qualitatively matching those of the experimental spectrum (Figure 4a).

The frequencies for the two low-frequency T_{2g} modes are very close to the experimental data, but those for the E_g and T_{2g} modes above 100 cm^{-1} are red-shifted slightly (about 10 cm^{-1}), as often seen in phonon analysis. The qualitative match of the experimental and DFT-calculated line positions (and relative intensities) allows a vibrational mode [$\nu(A_{1g})$, $\nu(E_g)$, $\delta(T_{2g})$, or $\nu^{\perp}(T_{2g})$] to be assigned to each experimental band, as summarized in Table 3. The Raman spectra are therefore consistent with the formation of Cs_2TeI_6 with $Fm\bar{3}m$ symmetry.

Figure 4b shows experimental FTIR reflectivity for Cs_2TeI_6 at 300 K. Two significant features emerge at 70 and 160 cm^{-1} . A low intensity shoulder near 170 cm^{-1} on the latter suggests

Table 3. Irreducible Representations, Optical Activities, and Vibrational Frequencies for the Cs_2TeI_6 Experimental and *Phonopy*-Calculated Zone-Center ($q=0$) Phonon Modes^a

type	modes	irrep	optical activity	ν_{DFT}^{\perp} (cm^{-1})	$\nu_{\text{expr.}}$ (cm^{-1})
acoustic	1, 2, 3	T_{1u}	silent	0.00	n/a
optical	4, 5, 6	T_{1g}	silent	12.95	n/a
	7, 8, 9	T_{2g}	Raman	35.08	27.10 (12)
	10, 11	T_{1u} TO	IR	38.08	62.6 (1.3) ^a
	12, 13, 14	T_{2u}	Silent	41.26	n/a
	15	T_{1u} LO	IR	45.99	94.6 (1.5) ^a
	16, 17, 18	T_{2g}	Raman	59.12	55.46 (4)
	19, 20	T_{1u} TO	IR	61.46	155.19 (16) ^a
	21	T_{1u} LO	IR	61.48	165.2 (5) ^a
	22, 23	E_g	Raman	107.41	97.73 (3)
	24	A_{1g}	Raman	121.76	111.212 (13)
	25, 26	T_{1u} TO	IR	162.01	171 (2)
	27	T_{1u} LO	IR	178.73	175.6 (1.8)

^aSee text for details.

that it is composed of multiple lines, as this line shape would not arise from a single simple absorption mode. As the factor group analysis indicates three IR-active T_{1u} vibrations, a reflectivity model using a Cs_2TeI_6 dielectric function employing three harmonic oscillators was fitted to the experimental spectrum. Each vibration would ordinarily be 3-fold degenerate, but their degeneracy is lifted as the vibration of one LO mode induces polarization that breaks the lattice periodicity (LO–TO splitting). This reflectivity fit finds transverse and longitudinal oscillation frequencies $\{\nu_{\text{TO}}, \nu_{\text{LO}}\}$ to be $\{62.6 (1.3), 94.6 (1.5)\}$, $\{155.19 (16), 165.2 (5)\}$, and $\{171 (2), 175.6(1.8)\}$ cm^{-1} , respectively, as given in Table 3. The DFT-calculated IR-active phonon relative optical absorption spectrum broadened using simulated 300 K line widths is presented in Figure 4b. (Note: the DFT spectrum is an

absorption instead of a reflectivity spectrum). As given in Table 3, the calculated three sets of transverse and longitudinal oscillation frequencies $\{\nu_{TO}, \nu_{LO}\}$ are $\{38.08, 45.99\}$, $\{61.46, 61.48\}$, and $\{162.01, 178.73\}$ cm^{-1} , respectively. The second pair of modes is invisible in Figure 4b as their calculated intensities are 100 times lower even than the minor mode at 38.08 cm^{-1} . Low-temperature FTIR reflectivity at 70 K verified the position and line shape of the highest frequency set of features but did not find any more convincing lines at lower energies for the other two sets, where the experimental spectrum is also rather noisy and may include features from the substrate. The discrepancy between the experimental and DFT IR-active lower energy phonon frequencies indicates that further work is necessary in evaluating the lower-energy region.

Properties of Cs_2TeI_6 Films Formed Using the Antisolvent Spin Method. Thermal stability is important for PV applications, and our investigation using combined DSC and TGA is shown in Figure 5, which includes scans for

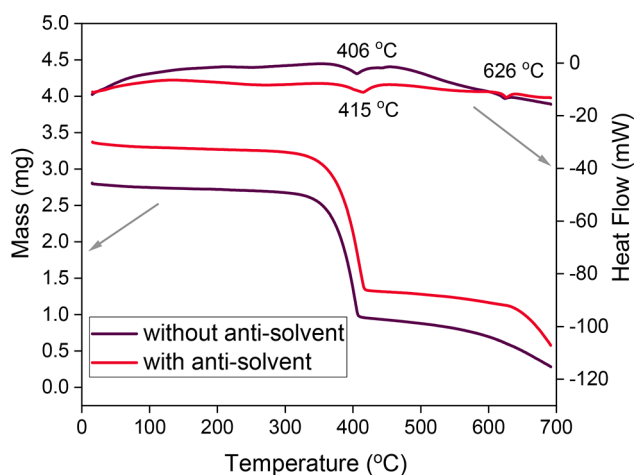


Figure 5. DSC and TGA results for Cs_2TeI_6 material prepared with the one-step process by spin coating from DMSO and with the inclusion of toluene as an antisolvent. Films prepared with the antisolvent appear to have higher stability, with the onsets of both mass loss and melting being shifted to slightly higher temperatures.

both one-step spin coated (from DMSO) and material prepared using toluene as an antisolvent. The TGA traces both show significant mass loss in the range 350–425 °C, while the DSC traces show melting (endothermic) transitions at 406–415 and 626 °C. Also, visual inspection of Cs_2TeI_6 films during annealing at 250 °C and above showed a change from black to white.

These observations are all consistent with the mass change being due to loss of TeI_4 , which is known to be volatile, a fact that we confirmed by DSC-TGA (Figure S4). This would leave a white or transparent film of the wide gap CsI which, by extrapolating vapor pressure data,³⁶ we expect to have an overpressure of just 0.019 Pa at 400 °C (Table S1). This residual material has a melting point on the DSC trace at 626 °C which is comparable to both the literature value of 621 °C for CsI³⁶ and our own value from DSC (Figure S5). Finally, we note that the onsets of both mass loss and melting are slightly higher for the films prepared with the toluene than without, which indicates that the denser material using antisolvent is the more thermally stable of the two.

Optical absorption measurements on Cs_2TeI_6 thin films were undertaken using UV–vis spectroscopy as shown in

Figure 6. The films made with all four antisolvents trialed (dichloromethane, diethyl ether, chlorobenzene, and toluene)

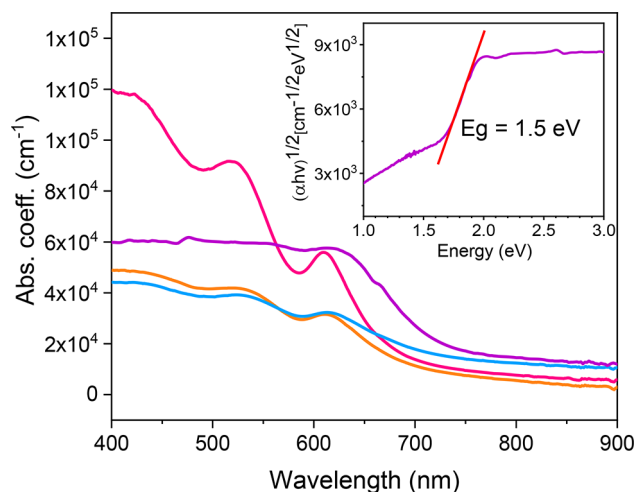


Figure 6. Absorption coefficients for Cs_2TeI_6 films prepared using the antisolvents: dichloromethane (pink), toluene (purple), diethyl ether (orange), and chlorobenzene (blue). The inset is Tauc plot of the film prepared with toluene and shows a band gap of 1.5 eV.

showed bandgap behavior with the onset of absorption being between 700–800 nm. Although reflectance was included in the calculations there were differences between the spectra which are most likely to be due to pinholes and surface morphology. For example, the spectra from the smoother films had interference fringes. Since absorption in this material is dominated by an indirect transition,¹⁷ the Tauc plot method (an extrapolation of $(\alpha h\nu)^{1/2}$ vs $h\nu$) was used to estimate the band gaps (Figure S6).³⁷ The plots had linear sections, and the film prepared using toluene indicated an optical gap of about 1.5 eV as shown in Figure 6.

The same result was found for films prepared by the one-step method (i.e., without the toluene antisolvent), and these values concur with two previous experimental studies reported of Cs_2TeI_6 which gave indirect band gaps of 1.59 and 1.50 eV.^{17,26} The absorption coefficient at 622 nm ($\sim 1.99 \text{ eV}$) was estimated to be $6.0 \times 10^4 \text{ cm}^{-1}$, which is of the same order of magnitude as the absorption coefficient for $\text{CH}_3\text{NH}_3\text{PbI}_3$. Hence although Cs_2TeI_6 is considered to be indirect gap material, it has sufficiently strong optical absorption to be viable as a solar absorber.

In order to estimate the work function of films of Cs_2TeI_6 and to investigate the electronic nature of the surface, we performed Kelvin probe measurements in the dark and under illumination. For a toluene antisolvent prepared film of Cs_2TeI_6 we determined a WF of 4.95 eV in the dark (details are given in the SI and Figure S7). Illumination generated a surface photovoltage (SPV) that was greater than the dark CPD value (Figure 7), and this is consistent with the surface of the material having p-type character.³⁸ (A schematic diagram is given in Figure S8.) We note that ref 17 speculates that Cs_2TeI_6 may be intrinsically n-type due to iodine vacancies but also that it may be unlikely in practice since V_i is predicted to be a deep rather than a shallow level and is therefore not expected to be ionized at room temperature. SPV measurements under varied intensity (Figure S8) showed relatively small increases in SPV < 100 mV, and this indicates that the density of the surface states could be low.

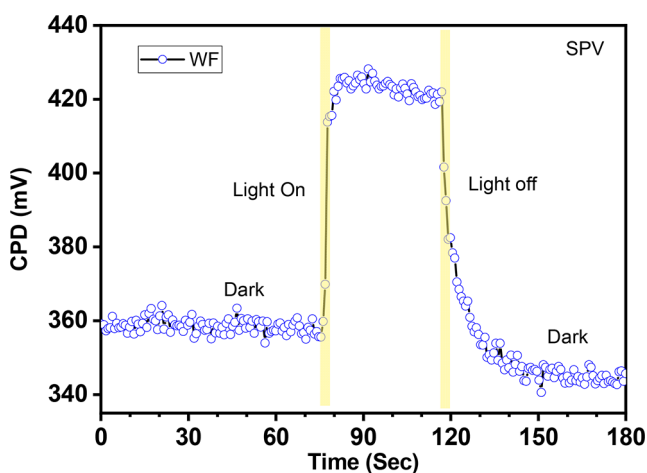


Figure 7. Surface photovoltage measurement of a film of Cs_2TeI_6 formed using the toluene antisolvent method. The increase in contact potential difference upon illumination indicates that the surface of the material has p-type character.

Carrier lifetimes in the films were estimated optically using a fluorescence lifetime imaging microscope system with a 480 nm laser excitation. Most often a three-term exponential was required to fit the decay curves, and this gave average lifetimes of 1.65 ± 0.45 ns for the one-step films and 2.60 ± 0.27 ns for the antisolvent spun films. A typical image and decay curve are shown in Figures S9 and S10, and the lifetimes are shown in Table S2. While the lifetimes are low in comparison with many bulk semiconductors and the fitting functions complex, this is likely to be because the samples are in thin film form (~ 200 nm thick) with free surfaces and no passivation. Indeed, the lifetimes measured for unpassivated surfaces of thin film CdTe are equally low, and yet the material is nevertheless successful as the active layer in high efficiency photovoltaic devices.

CONCLUSION

Spin coating stoichiometric amounts of CsI and TeI_4 in the ratio of 2:1 was shown to be able to produce films of Cs_2TeI_6 for the first time. Inclusion of toluene as an antisolvent during spin coating from DMSO followed by annealing at 110°C for 10 min yielded higher quality films than the simple one-step spin method without the antisolvent. The Cs_2TeI_6 ($Fm\bar{3}m$) phase was confirmed by XRD, with Rietveld analysis giving respective lattice parameters of 11.6775 and 11.6754 Å for films grown with and without antisolvent. The films were stable up to 250°C , above which they began to degrade by loss of TeI_4 , leaving a CsI residue. They showed optical gaps of ~ 1.5 eV and above-gap absorption coefficients of $\sim 6 \times 10^4$ cm^{-1} . Carrier lifetimes for unpassivated 200 nm thick films averaged 2.6 ns for antisolvent-spun films and 1.65 ns for one-step spin coating. Kelvin probe measurements indicated a work function of 4.95 eV, and surface photovoltage measurements indicate that the surface region is of p-type character. Experimental Raman and FTIR reflectivity spectra were analyzed alongside DFT *Phonopy*-calculated phonon spectra, which predicted the following optically active modes:

$$\Gamma_{\text{opt}}(k=0) = A_{1g}(\text{R}) + E_g(\text{R}) + 2T_{2g}(\text{R}) + 3T_{1u}(\text{IR})$$

Qualitatively matching experimental and *Phonopy* line positions and intensities further supported formation of the compound. This study has demonstrated the first formation of

thin films of Cs_2TeI_6 and surveyed their properties with the outcome that the material may now be investigated further as a potential optoelectronic material and an alternative for lead- and tin-containing perovskites in photovoltaics. Furthermore, alternative deposition methods including spray coating, slot-die coating, doctor blading, and screen- and inkjet-printing³⁹ could be investigated for larger scale fabrication of the films and devices.

EXPERIMENTAL AND COMPUTATIONAL DETAILS

One-Step Synthesis and Spin Coating of Cs_2TeI_6 Films on Quartz Glass Substrates. The film synthesis work was carried out under a nitrogen atmosphere with controlled levels of H_2O (<5 ppm). Cs_2TeI_6 was prepared by reacting CsI (Sigma-Aldrich, 99.999%) and TeI_4 (Alfa Aesar, 99%) in different solvents such as dimethyl sulfoxide (DMSO) and dimethylformamide (DMF). The films were deposited on ultraflat glass substrates coated with a 20 nm layer of synthetic quartz (20×15 mm^2). From the survey of experimental conditions for the formation of films, the following process was shown to be the optimum: CsI: TeI_4 (2:1 molar ratio) were mixed together in DMSO (53 wt %) in the glovebox. The best way to dissolve the reactants was by adding DMSO to CsI powder, stirring for 5 min, and adding TeI_4 to form a transparent solution. This was left stirring for 30 min at room temperature before filtering using a 0.22 μL PTFE filter. The resulting viscous and dark precursor solution was dynamically spin coated onto glass at 2000 rpm for 15 s in one step. Immediately after, the sample was placed on a hot plate at 100°C for 10 min. Two identical depositions were required to ensure a good quality film.

Characterization Methods. Scanning electron microscope (SEM) images and energy-dispersive X-ray spectroscopy (EDX) were taken using a JEOL 7001F with an acceleration voltage of 15 kV. Atomic force microscopy (AFM) was performed using a Veeco Innova Bruker instrument in contact mode. XRD patterns were recorded using a Rigaku SmartLab X-ray diffractometer in a parallel beam configuration. Rietveld refinement was carried out with the Fullprof suite.⁴⁰ Differential scanning calorimetry (DSC) was carried out under argon using a TA Instruments SDT Q600 with alumina crucibles with lids and a heating rate of $5^\circ\text{C}/\text{min}$. UV/vis spectra were taken using a Shimadzu Solid Spec 3700 UV-vis spectrophotometer and an integrating sphere, with the absorption coefficients being calculated taking into account both transmission and reflectance measurements. Fluorescence lifetime imaging microscopy (FLIM) was carried out at room temperature using a PicoQuant Micro Time 200 system with 480 nm laser excitation and a 776 nm cutoff filter. Raman spectra were measured by the Renishaw InVia Raman microscope with a 532 nm laser, a 50 \times objective lens, and 1 mW (0.5%) as the incident laser. Infrared specular reflection spectra were acquired at an 11° angle of incidence between ~ 40 and 1000 cm^{-1} at temperatures of 300 and 70 K using a Bruker Vertex 70v Fourier transform infrared (FTIR) spectrometer with a combined reflection-transmission accessory and an Oxford Instruments CFV2 continuous-flow helium cryostat.

Computational Details for Raman and IR Spectra Simulations. The second and third order force constants were calculated with the finite displacement method using *Phonopy* and *Phono3py*, based on forces evaluated by VASP (Vienna ab initio Simulation Package) on $2 \times 2 \times 2$ supercells (288 atom) and cubic conventional cells (36 atom), respectively. The macroscopic dielectric constant tensor for the pristine, as well as the Born, effective-charge tensors for both pristine and displaced (along the eigenvector of Raman active modes) primitive cells (9 atom) were calculated with density functional perturbation theory also using VASP. From the force constants, IR and Raman spectra are simulated using *Phonopy* spectroscopy, following Skelton et al.⁴¹ In all calculations, non-analytical correction to the dynamical matrix near the zone center was applied with the method of Gonze et al.^{42,43} Also, all calculations used the so-called PBEsol generalized-gradient-approximation (GGA) to exchange correlation functional.⁴⁴

■ ASSOCIATED CONTENT**SI Supporting Information**

The Supporting Information is available free of charge at <https://pubs.acs.org/doi/10.1021/acs.chemmater.0c02150>.

Schematic processing of Cs₂TeI₆ thin film preparation using the antisolvent method, Rietveld refinement, DFT calculated phonon dispersion, DSC-TGA data for precursors, Tauc plots, Kelvin probe contact potential difference, and fluorescence lifetime imaging microscopy (FLIM) measurements (PDF)

■ AUTHOR INFORMATION**Corresponding Author**

Isabel Vázquez-Fernández – Stephenson Institute for Renewable Energy, Department of Physics, University of Liverpool, Liverpool, United Kingdom; orcid.org/0000-0002-6466-4143; Email: vazquezfernandez@univ-tours.fr

Authors

Silvia Mariotti – Stephenson Institute for Renewable Energy, Department of Physics, University of Liverpool, Liverpool, United Kingdom; orcid.org/0000-0002-7163-9480

Oliver S. Hutter – Department of Mathematics, Physics and Electrical Engineering, Northumbria University, Newcastle upon Tyne NE1 8ST, United Kingdom; orcid.org/0000-0002-8838-8956

Max Birkett – Stephenson Institute for Renewable Energy, Department of Physics, University of Liverpool, Liverpool, United Kingdom; orcid.org/0000-0002-6076-6820

Tim D. Veal – Stephenson Institute for Renewable Energy, Department of Physics, University of Liverpool, Liverpool, United Kingdom; orcid.org/0000-0002-0610-5626

Theodore D. C. Hobson – Stephenson Institute for Renewable Energy, Department of Physics, University of Liverpool, Liverpool, United Kingdom; orcid.org/0000-0002-0013-360X

Laurie J. Phillips – Stephenson Institute for Renewable Energy, Department of Physics, University of Liverpool, Liverpool, United Kingdom; orcid.org/0000-0001-5181-1565

Lefteris Danos – Department of Chemistry, Lancaster University, Lancaster LA1 4YB, United Kingdom; orcid.org/0000-0001-7203-7206

Pabitra K. Nayak – Department of Physics, Clarendon Laboratory, University of Oxford, Oxford OX1 3PU, United Kingdom; TIFR Centre for Interdisciplinary Sciences, Tata Institute of Fundamental Research, Hyderabad 500107, India; orcid.org/0000-0002-7845-5318

Henry J. Snaith – Department of Physics, Clarendon Laboratory, University of Oxford, Oxford OX1 3PU, United Kingdom; orcid.org/0000-0001-8511-790X

Wei Xie – Department of Materials Science and Engineering, University of California, Berkeley, California 94720, United States; orcid.org/0000-0003-1501-896X

Matthew P. Sherburne – Department of Materials Science and Engineering, University of California, Berkeley, California 94720, United States; orcid.org/0000-0002-3992-1822

Mark Asta – Department of Materials Science and Engineering, University of California, Berkeley, California 94720, United States; orcid.org/0000-0002-8968-321X

Ken Durose – Stephenson Institute for Renewable Energy, Department of Physics, University of Liverpool, Liverpool, United Kingdom; orcid.org/0000-0003-1183-3211

Complete contact information is available at: <https://pubs.acs.org/doi/10.1021/acs.chemmater.0c02150>

Notes

The authors declare no competing financial interest.

■ ACKNOWLEDGMENTS

The authors acknowledge funding from EPSRC Grants EP/P02484X/1 and EP/L01551X/1 and support for the XRD facility under Grant EP/P001513/1. P.K.N. acknowledges the support via intramural funds at TIFR Hyderabad from the Department of Atomic Energy (DAE), India. The theoretical calculations were supported by the National Research Foundation (NRF), Singapore (CRP NRF2014-NRF-CRP002-036 and NRF-CRP14-2014-03), the Singapore–Berkeley Research Initiative for Sustainable Energy CREATE Program (W.X. and M.P.S.), and the U.S. Department of Energy, Office of Science, Office of Basic Energy Sciences, Materials Sciences and Engineering Division under Contract DE-AC02-05-CH11231 (Materials Project Program KC23MP) (M.A.).

■ REFERENCES

- (1) Kojima, A.; Teshima, K.; Shirai, Y.; Miyasaka, T. Organometal halide perovskites as visible-light sensitizers for photovoltaic cells. *J. Am. Chem. Soc.* **2009**, *131*, 6050–6051.
- (2) Lee, M. M.; Teuscher, J.; Miyasaka, T.; Murakami, T. N.; Snaith, H. J. Efficient hybrid solar cells based on meso-superstructured organometal halide perovskites. *Science* **2012**, *338*, 643–647.
- (3) Kim, H.-S.; Lee, C.-R.; Im, J.-H.; Lee, K.-B.; Moehl, T.; Marchioro, A.; Moon, S.-J.; Humphry-Baker, R.; Yum, J.-H.; Moser, J. E.; Grätzel, M.; Park, N.-G. Lead iodide perovskite sensitized all-solid-state submicron thin film mesoscopic solar cell with efficiency exceeding 9%. *Sci. Rep.* **2012**, *2*, 591.
- (4) NREL. *Best research-cell efficiency chart*. <https://www.nrel.gov/pv/cell-efficiency.html> (accessed 2020).
- (5) Mariotti, S.; Hutter, O. S.; Phillips, L. J.; Yates, P. J.; Kundu, B.; Durose, K. Stability and performance of CsPbI₂Br thin films and solar cell devices. *ACS Appl. Mater. Interfaces* **2018**, *10*, 3750–3760.
- (6) Yang, J.; Siempelkamp, B. D.; Liu, D.; Kelly, T. L. Investigation of CH₃NH₃PbI₃ degradation rates and mechanisms in controlled humidity environments using in situ techniques. *ACS Nano* **2015**, *9*, 1955–1963.
- (7) Sun, Q.; Fassl, P.; Becker-Koch, D.; Bausch, A.; Rivkin, B.; Bai, S.; Hopkinson, P. E.; Snaith, H. J.; Vaynzof, Y. Role of microstructure in oxygen induced photodegradation of methylammonium lead triiodide perovskite films. *Adv. Energy Mater.* **2017**, *7*, 1700977.
- (8) Niu, G.; Guo, X.; Wang, L. Review of recent progress in chemical stability of perovskite solar cells. *J. Mater. Chem. A* **2015**, *3*, 8970–8980.
- (9) Eperon, G. E.; Stranks, S. D.; Menelaou, C.; Johnston, M. B.; Herz, L. M.; Snaith, H. J. Formamidinium lead trihalide: a broadly tunable perovskite for efficient planar heterojunction solar cells. *Energy Environ. Sci.* **2014**, *7*, 982–988.
- (10) Rehman, W.; McMeekin, D. P.; Patel, J. B.; Milot, R. L.; Johnston, M. B.; Snaith, H. J.; Herz, L. M. Photovoltaic mixed-cation lead mixed-halide perovskites: links between crystallinity, photo-stability and electronic properties. *Energy Environ. Sci.* **2017**, *10*, 361–369.
- (11) Noh, J. H.; Im, S. H.; Heo, J. H.; Mandal, T. N.; Seok, S. I. Chemical management for colorful, efficient, and stable inorganic-organic hybrid nanostructured solar cells. *Nano Lett.* **2013**, *13*, 1764–1769.
- (12) Noel, N. K.; Stranks, S. D.; Abate, A.; Wehrenschnig, C.; Guarnera, S.; Haghighirad, A.-A.; Sadhanala, A.; Eperon, G. E.; Pathak, S. K.; Johnston, M. B.; Petrozza, A.; Herz, L. M.; Snaith, H. J.

Lead-free organic–inorganic tin halide perovskites for photovoltaic applications. *Energy Environ. Sci.* **2014**, *7*, 3061–3068.

(13) Lee, B.; Stoumpos, C. C.; Zhou, N.; Hao, F.; Malliakas, C.; Yeh, C.-Y.; Marks, T. J.; Kanatzidis, M. G.; Chang, R. P. H. Air-stable molecular semiconducting iodosalts for solar cell applications: Cs_2SnI_6 as a hole conductor. *J. Am. Chem. Soc.* **2014**, *136*, 15379–15385.

(14) Lee, B.; Krenselewski, A.; Baik, S. I.; Seidman, D. N.; Chang, R. P. H. Solution processing of air-stable molecular semiconducting iodosalts, $\text{Cs}_2\text{SnI}_{6-x}\text{Br}_x$ for potential solar cell applications. *Sustain Energy Fuels* **2017**, *1*, 710–724.

(15) Saparov, B.; Sun, J.-P.; Meng, W.; Xiao, Z.; Duan, H.-S.; Gunawan, O.; Shin, D.; Hill, I. G.; Yan, Y.; Mitzi, D. B. Thin-film deposition and characterization of a Sn-deficient perovskite derivative Cs_2SnI_6 . *Chem. Mater.* **2016**, *28*, 2315–2322.

(16) Qiu, X.; Jiang, Y.; Zhang, H.; Qiu, Z.; Yuan, S.; Wang, P.; Cao, B. Lead-free mesoscopic Cs_2SnI_6 perovskite solar cells using different nanostructured ZnO nanorods as electron transport layers. *Phys. Status Solidi RRL* **2016**, *10*, 587–591.

(17) Maughan, A. E.; Ganose, A. M.; Bordelon, M. M.; Miller, E. M.; Scanlon, D. O.; Neilson, J. R. Defect tolerance to intolerance in the vacancy-ordered double perovskite semiconductors Cs_2SnI_6 and Cs_2TeI_6 . *J. Am. Chem. Soc.* **2016**, *138*, 8453–8464.

(18) Serrano-Lujan, L.; Espinosa, N.; Larsen-Olsen, T. T.; Abad, J.; Urbina, A.; Krebs, F. C. Tin- and lead-based perovskite solar cells under scrutiny: an environmental perspective. *Adv. Energy Mater.* **2015**, *5*, 1501119.

(19) Mesquita, I.; Andrade, L.; Mendes, A. Perovskite solar cells: Materials, configurations and stability. *Renewable Sustainable Energy Rev.* **2018**, *82*, 2471–2489.

(20) Ba, L. A.; Döring, M.; Jamier, V.; Jacob, C. Tellurium: an element with great biological potency and potential. *Org. Biomol. Chem.* **2010**, *8*, 4203–4216.

(21) Grätzel, M. Recent advances in sensitized mesoscopic solar cells. *Acc. Chem. Res.* **2009**, *42*, 1788–1798.

(22) Hoefler, S. F.; Trimmel, G.; Rath, T. Progress on lead-free metal halide perovskites for photovoltaic applications: a review. *Monatsh. Chem.* **2017**, *148*, 795–826.

(23) Travis, W.; Glover, E. N. K.; Bronstein, H.; Scanlon, D. O.; Palgrave, R. G. On the application of the tolerance factor to inorganic and hybrid halide perovskites: a revised system. *Chem. Sci.* **2016**, *7*, 4548–4556.

(24) Taylor, A. Biochemistry of tellurium. *Biol. Trace Elem. Res.* **1996**, *55*, 231–239.

(25) Cai, Y.; Xie, W.; Ding, H.; Chen, Y.; Thirumal, K.; Wong, L. H.; Mathews, N.; Mhaisalkar, S. G.; Sherburne, M.; Asta, M. Computational study of halide perovskite-derived A_2BX_6 inorganic compounds: Chemical trends in electronic structure and structural stability. *Chem. Mater.* **2017**, *29*, 7740–7749.

(26) Peresh, E. Y.; Zubaka, O. V.; Sidei, V. I.; Barchii, I. E.; Kun, S. V.; Kun, A. V. Preparation, stability regions, and properties of M_2TeI_6 ($\text{M} = \text{Rb}, \text{Cs}, \text{Tl}$) crystals. *Inorg. Mater.* **2002**, *38*, 859–863.

(27) Burschka, J.; Pellet, N.; Moon, S.-J.; Humphry-Baker, R.; Gao, P.; Nazeeruddin, M. K.; Grätzel, M. Sequential deposition as a route to high-performance perovskite-sensitized solar cells. *Nature* **2013**, *499*, 316.

(28) Paek, S.; Schouwink, P.; Athanasopoulou, E. N.; Cho, K. T.; Grancini, G.; Lee, Y.; Zhang, Y.; Stellacci, F.; Nazeeruddin, M. K.; Gao, P. From nano- to micrometer scale: the role of antisolvent treatment on high performance perovskite solar cells. *Chem. Mater.* **2017**, *29*, 3490–3498.

(29) Mariotti, S.; Durose, K.; Major, J. D. *Hybrid and inorganic plumbo-halide perovskites for solar cells*, Ph.D. thesis. University of Liverpool, Liverpool, 2019.

(30) Rietveld, H. M. A profile refinement method for nuclear and magnetic structures. *J. Appl. Crystallogr.* **1969**, *2*, 65–71.

(31) Kim, K. H.; Chun, J. S. X-ray studies of SnO_2 prepared by chemical vapour deposition. *Thin Solid Films* **1986**, *141*, 287–295.

(32) Andrews, R. L.; Heyns, A. M.; Woodward, P. M. Raman studies of A_2MWO_6 tungstate double perovskites. *Dalton Trans.* **2015**, *44*, 10700–10707.

(33) Jain, A.; Ong, S. P.; Hautier, G.; Chen, W.; Richards, W. D.; Dacek, S.; Cholia, S.; Gunter, D.; Skinner, D.; Ceder, G.; Persson, K. A. Commentary: the materials project: a materials genome approach to accelerating materials innovation. *APL Mater.* **2013**, *1*, No. 011002.

(34) Togo, A.; Tanaka, I. First principles phonon calculations in materials science. *Scr. Mater.* **2015**, *108*, 1–5.

(35) Kaltzoglou, A.; Antoniadou, M.; Kontos, A. G.; Stoumpos, C. C.; Perganti, D.; Siranidi, E.; Raptis, V.; Trohidou, K.; Psycharis, V.; Kanatzidis, M. G.; Falaras, P. Optical-vibrational properties of the Cs_2SnX_6 ($\text{X} = \text{Cl}, \text{Br}, \text{I}$) defect perovskites and hole-transport efficiency in dye-sensitized solar cells. *J. Phys. Chem. C* **2016**, *120*, 11777–11785.

(36) Lide, D. R. *CRC Handbook of Chemistry and Physics*; CRC press: Boca Raton, FL, 2004; Vol. 85.

(37) Tauc, J. Optical properties and electronic structure of amorphous Ge and Si. *Mater. Res. Bull.* **1968**, *3*, 37–46.

(38) Schutt, K.; Nayak, P. K.; Ramadan, A. J.; Wenger, B.; Lin, Y.-H.; Snaith, H. J. Overcoming zinc oxide interface instability with a methylammonium-free perovskite for high-performance solar cells. *Adv. Funct. Mater.* **2019**, *29*, 1900466.

(39) Liu, C.; Cheng, Y.-B.; Ge, Z. Understanding of perovskite crystal growth and film formation in scalable deposition processes. *Chem. Soc. Rev.* **2020**, *49*, 1653–1687.

(40) Rodríguez-Carvajal, J. Recent advances in magnetic structure determination by neutron powder diffraction. *Phys. B* **1993**, *192*, 55–69.

(41) Skelton, J. M.; Burton, L. A.; Jackson, A. J.; Oba, F.; Parker, S. C.; Walsh, A. Lattice dynamics of the tin sulphides SnS_2 , SnS and Sn_2S_3 : vibrational spectra and thermal transport. *Phys. Chem. Chem. Phys.* **2017**, *19*, 12452–12465.

(42) Gonze, X.; Charlier, J. C.; Allan, D. C.; Teter, M. P. Interatomic force constants from first principles: The case of α -quartz. *Phys. Rev. B: Condens. Matter Mater. Phys.* **1994**, *50*, 13035–13038.

(43) Gonze, X.; Lee, C. Dynamical matrices, Born effective charges, dielectric permittivity tensors, and interatomic force constants from density-functional perturbation theory. *Phys. Rev. B: Condens. Matter Mater. Phys.* **1997**, *55*, 10355–10368.

(44) Perdew, J. P.; Ruzsinszky, A.; Csonka, G. I.; Vydrov, O. A.; Scuseria, G. E.; Constantin, L. A.; Zhou, X.; Burke, K. Restoring the density-gradient expansion for exchange in solids and surfaces. *Phys. Rev. Lett.* **2008**, *100*, 136406.